



# Dual-Energy: The Philips Approach

Ami Altman, Galit Kafri, and Sary Shenhav

## Contents

1	<b>Spectral Detection Through a Dual-Layer Detector</b> .....	30
2	<b>Spectral Material Decomposition and Reconstruction</b> .....	31
3	<b>Spectral Results</b> .....	34
3.1	MonoE: Monoenergetic Images [HU].....	34
3.2	VNC: Virtual Non-Contrast.....	36
3.3	Iodine No Water [mg/ml].....	37
3.4	Calcium Suppression [HU].....	37
3.5	Iodine Density [mg/ml].....	38
3.6	Contrast-Enhanced Structures [HU].....	38
3.7	Iodine Removed [HU].....	39
3.8	Uric Acid and Uric Acid Removed Pair [HU].....	39
3.9	Z Effective.....	40
3.10	Electron Density [%EDW].....	40
	<b>References</b> .....	42

## Abstract

The Philips dual-layer detector approach for spectral imaging was introduced as early as 2005 in a prototype installed in Hadassah University Medical Center, Israel. Since then both the detector design and the material decomposition and reconstruction techniques were further developed and improved to allow better SNR and CNR in spectral results. This

single-source approach to spectral imaging has some clear advantages: energies acquisition is perfectly aligned by design; it does not require a special dual-energy acquisition mode thus making all scans spectral and enables projection-based material decomposition. It also allows for advanced clinical application, such as cardiac and perfusion, to utilize spectral imaging. In addition, it allows to easily overcome limitations of the source-based techniques in the sense that it does not have dose penalties, field of view restriction, it does not require to slow rotation time, and it is not limited by patient habitus.

A. Altman · G. Kafri · S. Shenhav (✉)  
Philips Medical Systems Technologies Ltd.,  
Advanced Technologies Center, Haifa, Israel  
e-mail: [sary.shenhav@philips.com](mailto:sary.shenhav@philips.com)

In this chapter, we will discuss the dual-layer detector architecture, projection-based material decomposition and image reconstruction as well as the different spectral results and their clinical use.

## 1 Spectral Detection Through a Dual-Layer Detector

While material decomposition in energy-selective CT was proposed by Alvarez and Macovski in 1976, a dual-layer detector for a simultaneous acquisition of two energies in CT was first proposed by Brooks and Di Chiro in 1978. A Philips Healthcare team proposed a different configuration and implementation of that idea (Carmi et al. 2005; Altman et al. 2006) and in October 2005 Philips has installed the world first clinical prototype utilizing a single-source spectral detection technique at the Hadassah Medical Center in Jerusalem, Israel. This implementation included two attached scintillator layers, optically separated, and read by a side-looking, edge-on, silicon photodiode, thin

enough to maintain the same detector pitch and geometrical efficiency as a conventional CT detector (Figs. 1 and 2). The top scintillator layer's atomic number and thickness have been optimized to maximize energy separation at 120 and 140 kVp, while maintaining high enough signal statistics for the low-energy raw data even for a large patient. A low Z (atomic number) Garnet scintillator material, with a high light-output (~15%–20% better than GOS), has been developed to meet these requirements. This contributes to a high SNR in the top (low-energy) layer detector, enabling it to function at a very low dose without causing artifacts, typical to electronic-noise dominant signals.

The mean energy separation of the dual-layer detector, at 120 kVp, with and without a 30-cm water absorber, is shown in Fig. 3. The decrease in energy separation with increasing patient size is compensated due to the complete consistency in sampling of the two energies.

The Philips approach to spectral imaging is unique in the sense that it is based on a single source and spectral detection. Compared to source-based dual-energy techniques, the detector-based technique has some clear advan-

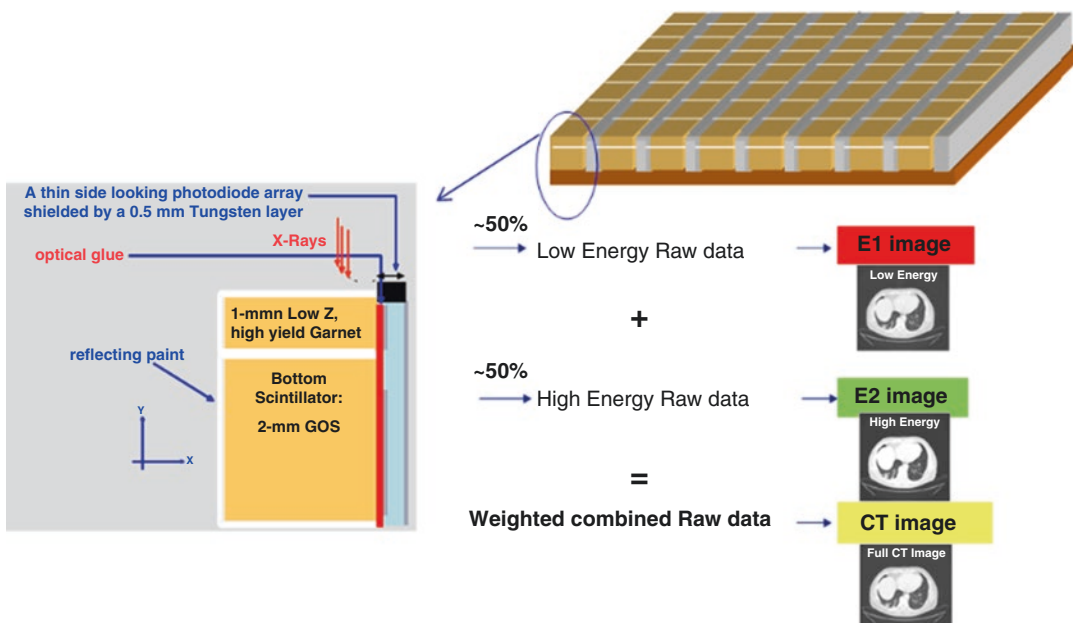


**Fig. 1** A schematic view of the Philips Healthcare dual-layer detector

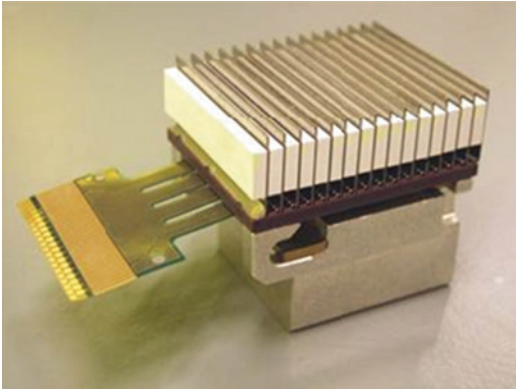


**Fig. 2** A vertical implementation of a  $16 \times 16$  pixels dual-layer detector

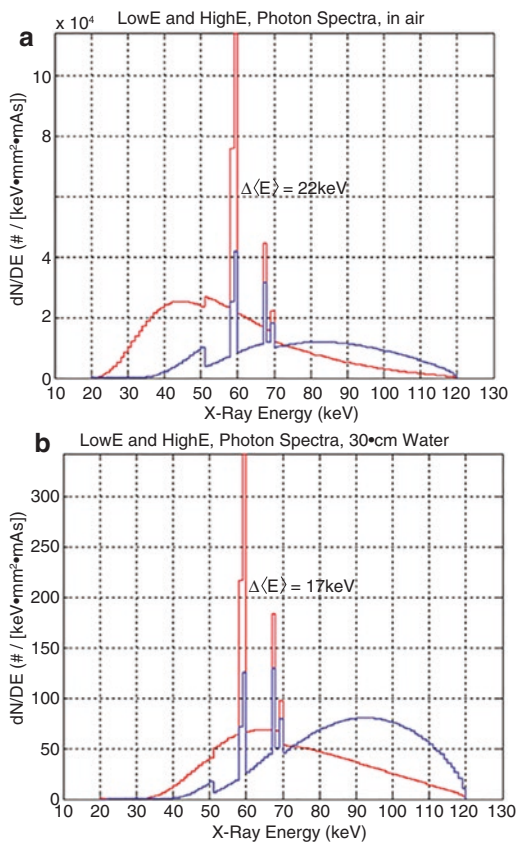


**Fig. 3** Top and bottom layers' spectra and mean energy difference in air (a) and with 30-cm water absorber (b), for 120 kVp

tages: energies acquisition is perfectly aligned by design as they are not only simultaneously measured, but also sampled exactly at the same angle at the same pixel, unlike the other methods of dual-energy CT; it does not require a special dual-energy acquisition mode thus making all scans spectral and enables projection-based material decomposition (see next section) which in turns allows better SNR and CNR in spectral results, like iodine quantification, effective atomic number image, electron densities, and virtual MonoE images (Sellerer et al. 2018; Ehn et al. 2018). It also allows for advanced clinical application, such as cardiac and perfusion, to utilize spectral imaging. In addition, it allows to easily overcome limitations of the source-based techniques in the sense that it does not have dose penalties, field of view restriction, it does not require to slow rotation time and it is not limited by patient habitus.

## 2 Spectral Material Decomposition and Reconstruction

Dual-energy spectral decomposition in the projection domain, using a two-base model, was first proposed by Alvarez and Macovski (1976). In this approach, the two projections data sets of the low and high energies are transformed into a new pair of projections data sets, from which all the various spectral results can be derived. The resulting two spectral-projections data sets are independent of the incident spectrum, hence clear from beam hardening effect, while even metal beam hardening and artifacts can be suppressed quite easily. This is a very important result of the projection-domain spectral decomposition, unlike image-domain spectral decomposition, where the resulting spectral images (e.g., virtual monochromatic images) suffer from beam hardening effects, and require special beam hardening correction, which is, often, insufficient (see e.g., Carmi et al. 2005).

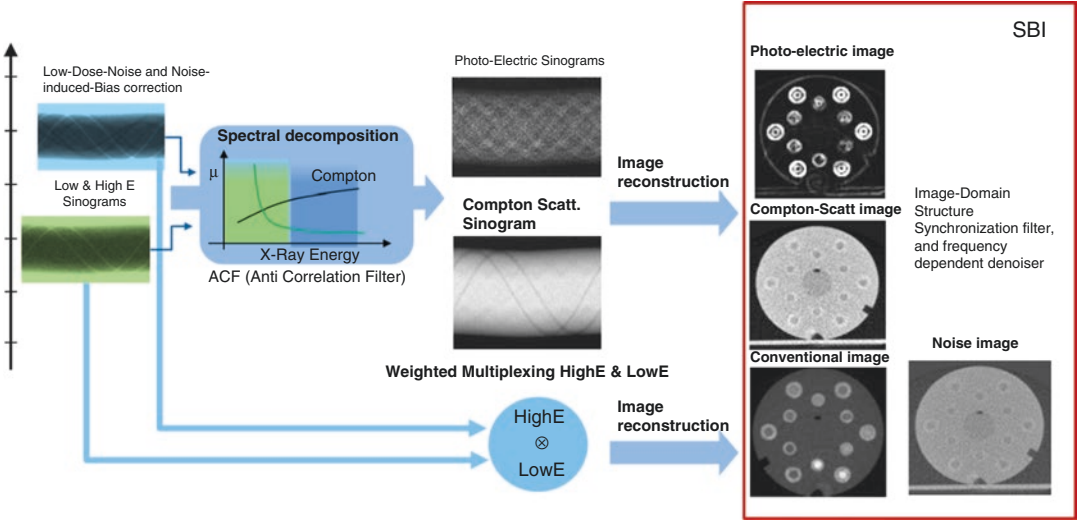


**Fig. 4** A schematic description of the Philips spectral decomposition and image reconstruction

The Philips implementation of projection-domain spectral decomposition (Altman et al. 2015) assumes an accurate forward model of the projection’s formation, as an input. This includes the precise source X-ray spectrum, the beam filtration, its variations in the directions to all the detection pixels, and the resulting different spectrum incident on each detection pixel in air. This implementation is simpler than the empirical approach proposed in (Alvarez and Macovski 1976), or the maximum-likelihood method proposed by Alvarez (Alvarez et al. 2011).

The basic Philips approach to the transformation from the **low** and **high energies** projections data sets to the Photo-Electric and Compton-scattering projections data sets is described below in Fig. 4 and the following equations:

$$\begin{aligned} \left\{ P_{\text{high}} \right\}, \left\{ P_{\text{low}} \right\} &\Rightarrow \left\{ P_{\text{scatt.}}^M \right\}, \left\{ P_{\text{photo}}^M \right\} \\ \text{Spectrum dependent} &\quad \text{Spectrum independent} \\ &= \mu_0 \cdot \left\{ a_{\text{scatt.}}^M \right\}, \mu_0 \cdot \left\{ a_{\text{photo}}^M \right\} \end{aligned}$$

where  $\mu_0$  is an arbitrary quantity with a dimension of an attenuation coefficient, which the end results are divided by at the end of the process.

The above transformation utilizes a two-base model:

$$\begin{aligned} \mu^M(E) &= \mu_{sc}^M(E) + \mu_{ph}^M(E) \cong f_{sc}(E) \cdot \mu_{sc}^M(Z_\xi, \rho_\xi) \\ &\quad + f_{ph}(E) \cdot \mu_{ph}^M(Z_\xi, \rho_\xi) \end{aligned}$$

where M represents a material mix, optimized for energy-dependence “universality” (~71% soft tissue, ~28% bone, ~1% iodine), while assuming the following:

1. Variable separation between the energy dependence and the Z dependence of the attenuation coefficient components (cross sections) is possible within the X-rays energy range used in CT.
2. The energy dependence of Compton Scattering, and the Photo-Electric cross sections, can be considered to be the same for all patients and test phantoms, based on the above material mix (this excludes phantoms and objects with a very large content of heavy metals/elements).
3. Coherent scattering can be either neglected or included in the photo-electric component (Energy dependence is  $\sim 1/E^2$ ).

Assuming the above, the line integrals can be expressed as:

$$\int \mu(\xi, E) d\xi \cong f_{scat}^M(E) \cdot \int \mu_{scat}^M(\xi) d\xi + f_{phot}^M(E) \cdot \int \mu_{phot}^M(\xi) d\xi$$

$$\boxed{= a_{scat}^M} \qquad \boxed{= a_{phot}^M}$$

$$P_{h,l} = -\log \left( \frac{\int_0^\infty \exp(-\int \mu(\xi, E) d\xi) \cdot F_{h,l}(E) \cdot EdE}{\int_0^\infty F_{h,l}(E) \cdot EdE} \right)$$

and the projections value for each line integral (detection pixel) can be obtained:

$$P_{h,l} = -\log \left( \frac{\int_0^\infty \exp(-f_{scat.}(E) \cdot a_{scat}^M - f_{phot}(E) \cdot a_{phot}^M) \cdot F_{h,l}(E) \cdot EdE}{\int_0^\infty F_{h,l}(E) \cdot EdE} \right)$$

From which, the values of  $a_{scat}^M$  and  $a_{phot}^M$ , the spectral line integrals are derived.

Where,

1. The functions  $f_{phot}(E)$  and  $f_{scat}(E)$  are derived from the E dependence of the chosen material mix M, calculated from NIST tables.
2.  $F_l(E)$  and  $F_h(E)$  are the energy distributions of the X-ray beam in air, incident on the top layer pixels and the bottom layer pixels, respectively (after all filtration and without any scanned object/body). Note that both  $F_l(E)$  and  $F_h(E)$  are matrices of distribution functions that must be pre-calculated and require full input/knowledge of the filtration along the rays to each detector pixel.
3. The material decomposition procedure described above has two important "side effects" that are addressed:
  - (a) Anti-correlated Noise: The transformation, mentioned above, determines the specific portions of LowE signal and HighE signal, assigned to the Scatter and to the Photo projection signals, respectively. As a result any portion of a radiation signal that is assigned to the Scatter projection signal, while it should have been assigned to the Photo signal, would cause a correlated error in the correspond-

ing Photo-Electric signal, and vice versa. This would result in a correlated noise between the two, hence would need a special consideration of how to reduce this noise through an Anti-Correlation Filter (ACF) in the projection domain.

- (b) Noise Induced Bias: It occurs in many cases, since the original radiation intensity per detection pixel is divided between two separate projection signals (Scatter and Photo projections sets in Philips approach). In this case, taking the logarithm of the raw signal, the statistical uncertainty of which is at the tail of the Poisson distribution, is causing a DC bias. This bias is corrected by a special filter at the input to the material decomposition process.
4. Following the reconstruction of the Photo-Electric and the Scatter images, special filters/algorithms are used, in the image domain, to conserve image structures, edges, and features, adapted from the conventional image, while reducing the image noise in a frequency-dependent form.

It is important to emphasize that projection-domain spectral decomposition can be used only if the signals from the two X-ray energies are

sampled both simultaneously (“Equi-time”) and at the same angle (“Equi-angle”). Only the spectral-detector and the fast-kVp-switching methods meet this condition.

### 3 Spectral Results

The Philips spectral CT system can provide a variety of spectral image types, on top of the conventional images, which are reconstructed through advanced spectral algorithms. Those spectral results can be generated either prospectively, on the scanner and sent to PACS, or retrospectively, directly on PACS utilizing Spectral Based Images known as SBI (as described above) and have the potential for additional clinical information to conventional CT imaging. Each spectral result is designed for a different clinical usage as will be explained in this chapter.

As described above, data from the low and high energy layers of the spectral detector undergo spectral decomposition in the projection space to generate optimal photo-electric absorption and Compton scattering images that are used as a two-base model. These optimal photo-electric absorption and Compton scattering images do not represent the pure Compton and photo-electric effects. They are slightly modified version of them. This is because different materials have slightly different energy dependencies, mainly at low energies, from the expected theoretical models of the two basic physical interactions. Moreover, coherent scattering which is the third component that contributes to the total attenuation of X-ray in matter need to be included, despite its relatively small contribution.

The optimal Photo and Scatter sets of images are stored together with the derived noise-images set in a special SBI (Spectral Based Images) format. All the relevant spectral results and images can be derived from the SBI series, using various algorithms. Hence, the spectral results can be created on demand and reviewed as needed on PACS and are not required to be sent to PACS prospectively.

The conventional images are analogous to the images obtained from a single-energy scanner

and are utilized for routine diagnostic purposes. For every scan, the pre reconstructed sum of the signals from the simultaneous acquisition of the high- and the low-energy data is combined to obtain the total amount of absorbed energy. Filtered back projection or iterative reconstruction algorithms are then used to reconstruct the combined raw data and create true conventional images. It has been shown that image quality of these conventional images from the Philips spectral CT system are comparable to images obtained from a single-energy scanner (Hojjati et al. 2017; Van Ommen et al. 2018).

Spectral results can have units of attenuation (HU) and other voxel values that represents physical quantities, for example, density in mg/ml. The clinical use of the different spectral results generated from the spectral-detector DECT have been demonstrated in several papers for several clinical applications in body, cardiac and neuro imaging (Brun Andersen et al. 2020; Fulton et al. 2017; Rajiah et al. 2017a; Neuhaus et al. 2017a) as well as for emergency imaging (Demirler Simsir et al. 2020). The high quantitative accuracy of the various spectral results was recently demonstrated in several studies (Ehn et al. 2017; Hua et al. 2018).

In the following, the algorithm and the potential clinical usage of the different spectral results will be discussed.

#### 3.1 MonoE: Monoenergetic Images [HU]

MonoE images are virtual mono-energy images which simulate images as if they are obtained using a pure monochromatic X-ray beam at a specific keV value. Virtual monochromatic images are generated between 40 keV and 200 keV, in increment of 1 keV, and the voxels in these images represent Hounsfield values (HU). This is illustrated in Fig. 5. The MonoE images are created by a linear combination of the two-base model, namely the photo-electric effect (PE) and Compton scattering (Sc) components, where a different weight is used for each KeV. In the low energy range the proportion of the photo-

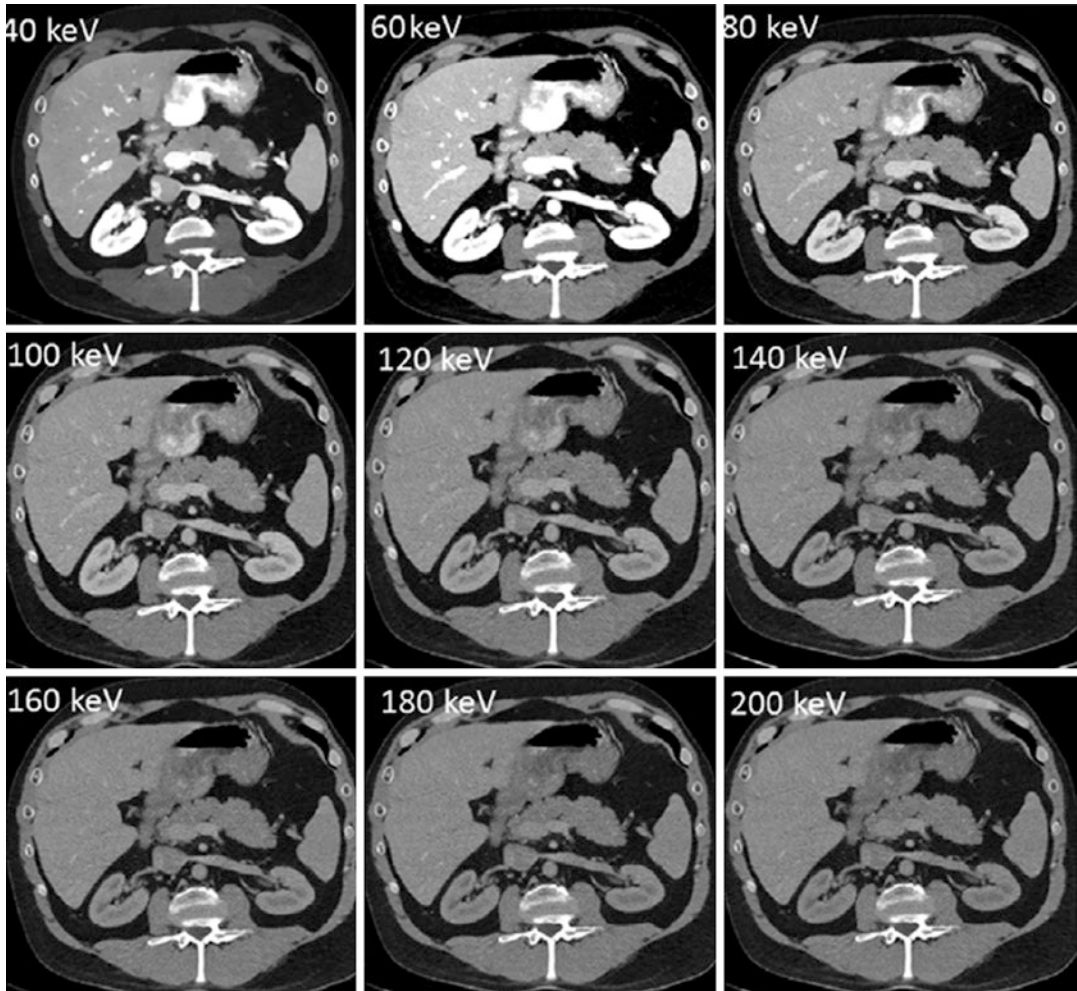


**Fig. 5** Virtual mono-energetic images from 40 to 200 keV displaying tissue attenuation properties similar to those resulting from imaging with a mono-energetic beam at a single keV level (Fulton et al. 2017)

electric effect is high and the Compton scattering is low, whereas in the high energy range it is opposite. In the 70 keV the proportions of these two components are very similar.

It should be noted that it is possible to generate monoE results also for keV values higher than the used kVp value since the behavior of the universal energy dependent basis is known also for high energies. Also, in order to stay above the K-edge of Iodine (33.2 keV), the lowest monoE was selected to be 40 keV.

In the Philips spectral CT system, the noise in the spectral results is typically lower than in the

corresponding conventional images due to special noise reduction techniques that are used in the spectral reconstruction process to minimize the noise and to optimize the signal to noise ratio (Kaltsz et al. 2017). See also Spectral Material Decomposition and Reconstruction section above.

A specific result named mono E-equivalent to conventional CT can be generated as well. This result has almost the same HU value as a conventional image generated from 120 kVp voltage (regardless of the actual tube voltage used during the scan) but with lower artifacts and noise.

The equivalent monochromatic images are 70 keV, 66 keV, and 64 keV for body, head, and extremities, respectively.

Monochromatic images may overcome some of the limitations of a polychromatic X-ray beam. A conventional CT image is created from a poly-energetic X-ray tube with a certain voltage (e.g., 120 kVp, 140 kVp) and therefore it is reconstructed from multiple energies. Since the mono-energetic series (MonoE) represents a single energy, it minimizes some of the known limitations of a polychromatic X-ray beam. For example, beam-hardening, metallic, and calcium blooming artifacts.

The potential benefits of the high virtual mono-energetic images derived from dual-layer CT scans for reduction of artifacts caused by orthopedic metal implants, were demonstrated both in a phantom study (Wellenberg et al. 2017) and clinical studies for implants in the spine, pelvis, and extremities (Neuhaus et al. 2017b; Große Hokamp et al. 2017a) as well as dental implants (Große Hokamp et al. 2018).

Low-energy mono-energetic images are influenced by photo-electric data, resulted in increasing attenuation and signal to noise ratio (SNR) and are therefore useful for all vascular imaging. The increased attenuation at low keVs can be used for contrast reduction, which is especially important in patients with renal insufficiency (Oda et al. 2018; Tsang et al. 2017; Nagayama et al. 2017; Hickethier et al. 2020) and for improvement in image quality when the contrast enhancement is suboptimal, salvaging angiographic studies and reducing the need for additional contrast or radiation dose. Also, low MonoE reconstructions allow the user to create angiography studies from a routine contrast-enhanced exam, adding additional diagnostic information to the exam. In addition, low MonoE images are used for better lesion conspicuity (Liu et al. 2019; Yoon et al. 2020; Große Hokamp et al. 2017b).

The advantage of the monochromatic images was also demonstrated in neuroimaging by reducing beam hardening artifacts for optimized gray-white matter contrast (Neuhaus et al. 2017c) and for visualization improvement of intracranial

hemorrhage and brain lesions (Lennartz et al. 2018). In addition, it was demonstrated that improved gray-white matter differentiation in cranial CT by using virtual mono-energetic images enables a radiation dose reduction compared to conventional images (Reimer et al. 2019). The reduction of blooming artifacts for coronary stent assessment and calcium blooming reduction in cardiac imaging was recently demonstrated as well (Hickethier et al. 2017; Van Hedent et al. 2018).

The next spectral results that are described are the virtual non-contrast (VNC), iodine no water, and calcium suppressed. These three spectral types belong to the same category of two-material decomposition. A two-material decomposition algorithm assumes that each voxel consists of two types of materials only. In order to achieve this, a simple linear basis transformation from the basis of the photo-electric effect and Compton scattering components into a new basis representation of two selected materials is performed. By selecting the two materials to be iodine and water, it is possible to generate the virtual non-contrast (VNC) and the iodine no water results. By selecting the materials to be a calcium-based material and water, a calcium suppressed image can be created.

### 3.2 VNC: Virtual Non-Contrast

This is a spectral result that mimics the attenuations values of a non-contrast CT scan from a data that is acquired with a contrast injection. It thus has the potential of replacing a true non-contrast series. By applying the two-materials decomposition to a NIST-based iodine and water basis, the iodine attenuation contribution of each voxel is removed and only the water attenuation contribution of each voxel in HU is displayed according to the mono 70 keV image. Due to the nature of this algorithm, the HU of the bony structures and calcium pixels are decreased by about 50% of their value in the 70 keV image.

A recent study compared the VNC images derived from the dual-layer spectral detector to a true non-contrast (TNC), found a good agree-



ment of the attenuation measurements between the two images in most abdominal tissues with an overestimation in fatty tissues (Jamali et al. 2019). This is in agreement with prior studies (Ananthakrishnan et al. 2017; Sauter et al. 2018) where the quality of iodine removal in VNC images was not influenced by the original contrast enhancement and thus has a potential advantage in reducing the radiation dose delivered to the patient in biphasic and triphasic examinations.

It was also shown that with an appropriately chosen proportionality factor as a correction coefficient, spectral CT VNC can reliably estimate the calcium score from a contrast-enhanced coronary CTA and shows good agreement with the conventional technique (Nadjiri et al. 2018).

### 3.3 Iodine No Water [mg/ml]

This is a spectral result type in which the voxel values represent the iodine concentration of the displayed tissue in mg/ml as calculated from the iodine-water two-material decomposition algorithm. The quantification of the iodine density is calculated by scaling the iodine projection on the water basis. Non-enhanced soft tissues are set to approximately 0 mg/ml of iodine.

Iodine no water [mg/ml] images have the potential to allow for improved visualization of iodine-enhanced tissues. This result can also be used for iodine quantification, but only in areas where iodine is present.

The accuracy of the iodine concentrations was tested in a phantom study for a range of concentrations between 2 and 20 mg/ml and found to be within a 0.3 mg/ml accuracy (Hua et al. 2018).

In Fig. 6, we show an example where a conventional, VNC, and iodine no water images are compared for a renal lesion.

### 3.4 Calcium Suppression [HU]

In this image type, voxels containing calcium are suppressed and replaced by virtual HU values as similar as possible to the expected HU without calcium contribution to the attenuation. In a similar way to the VNC algorithm, the contribution of the calcium-based material attenuation of each voxel is removed and only the water attenuation contribution of each voxel is displayed in HU according to the mono 70 keV. In contrast to VNC algorithm, where the iodine material is represented by a specific slope, the bony structures cannot be represented by one slope but of a range of calcium-based materials slopes. According to

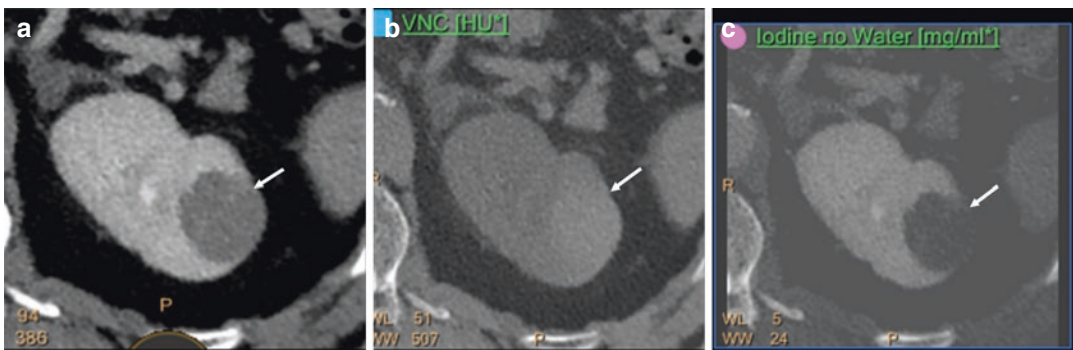


**Fig. 6** (a) Axial CT scan at the level of left kidney shows a cystic lesion, which has attenuation higher than a simple cyst (arrow); (b) virtual non-contrast CT at the same level shows that there is higher attenuation in the VNC image indicating that this is a hemorrhage; and (c) iodine-only

image at the same level shows absence of significant iodine in the lesion thus confirming that there was no contrast uptake in the lesion, but the high attenuation is consistent with hemorrhage, thus a complicated cyst (Fulton et al. 2017)

the calcium composition weight in each bony structure, an appropriate index value can be selected. A low index value selection targets tissues with a low calcium composition weight; a high index value selection targets tissues with a high calcium composition weight.

In a recent study, the calcium suppressed images from dual-layer CT have been used to visualize the bone marrow edema in traumatic vertebral compression fractures (Neuhaus et al. 2018). In a different study (Abdullayev et al. 2019), it was found that calcium suppressed images are capable of improving differentiation between a metastatic and a normal bone. Also, it was demonstrated that calcium suppressed images could clearly present the temporomandibular joint displacement. This suggested that calcium suppressed images could be used to diagnose the displacement of the temporomandibular joint disc (Zhang et al. 2020).

In the above described spectral types, where the two-material decomposition is applied, the algorithm didn't attempt to separate between two selected materials. In the spectral results that are explained below, a classification method between two materials is performed. The spectral results that are included in this category are the iodine density, contrast-enhanced structures, iodine removed, and the pair uric acid and non-uric acid removed.

### 3.5 Iodine Density [mg/ml]

This is an image type in which, similarly to the iodine no water result, the voxels values represent the iodine concentration of the displayed tissue in mg/ml. In this image, the non-negative iodine quantification for all voxels which are classified as including Iodine is calculated by scaling the iodine projection on the water basis as explained for the iodine no water result. Voxels which are classified as not included iodine are set to 0 mg/ml and are visualized as black pixels.

Similar to the iodine no water result, iodine density images enable the identification of

iodine-containing structures as well as direct quantification of iodine.

The accuracy of the iodine concentrations for iodine density was tested in a phantom study for a range of concentrations between 2 and 20 mg/ml and found to be within a 0.3 mg/ml accuracy (Hua et al. 2018).

It was shown that iodine density allows one to detect occult bone lesions that cannot be detected with conventional CT due to the high contrast of the bone and the lack of bone destructions. Iodine density yields high sensitivity and adequate specificity for the differentiation of vertebral trabecular metastases and healthy trabecular bone (Borggreffe et al. 2019). In another study (Kikano et al. 2020), it was shown that iodine density images can help elucidate and differentiate between various cardi thoracic pulmonary perfusion anomalies and may enhance a radiologist's diagnostic confidence. Also, Lennartz et al. showed that iodine overlay images obtained with spectral-detector CT improve visual and quantitative diagnostic accuracy in assessing skeletal muscle metastases compared to conventional images (Lennartz et al. 2019). In a study case, iodine density images allowed for differentiation of benign and malignant pulmonary nodules (Große Hokamp et al. 2019).

In Fig. 7, we show hypodense lesion in the head of the pancreas using conventional CT, mono-energetic 40 KeV, iodine density, and Z effective. The Z effective result will be discussed shortly.

### 3.6 Contrast-Enhanced Structures [HU]

In this result all the voxels, which are classified as including iodine, remain identical to MonoE 70 keV. All bone classified voxels are displayed as black voxels. Contrast-enhanced structures images have the potential of providing bone-free images which can help in visualizing vascular structures without bone or calcifications.

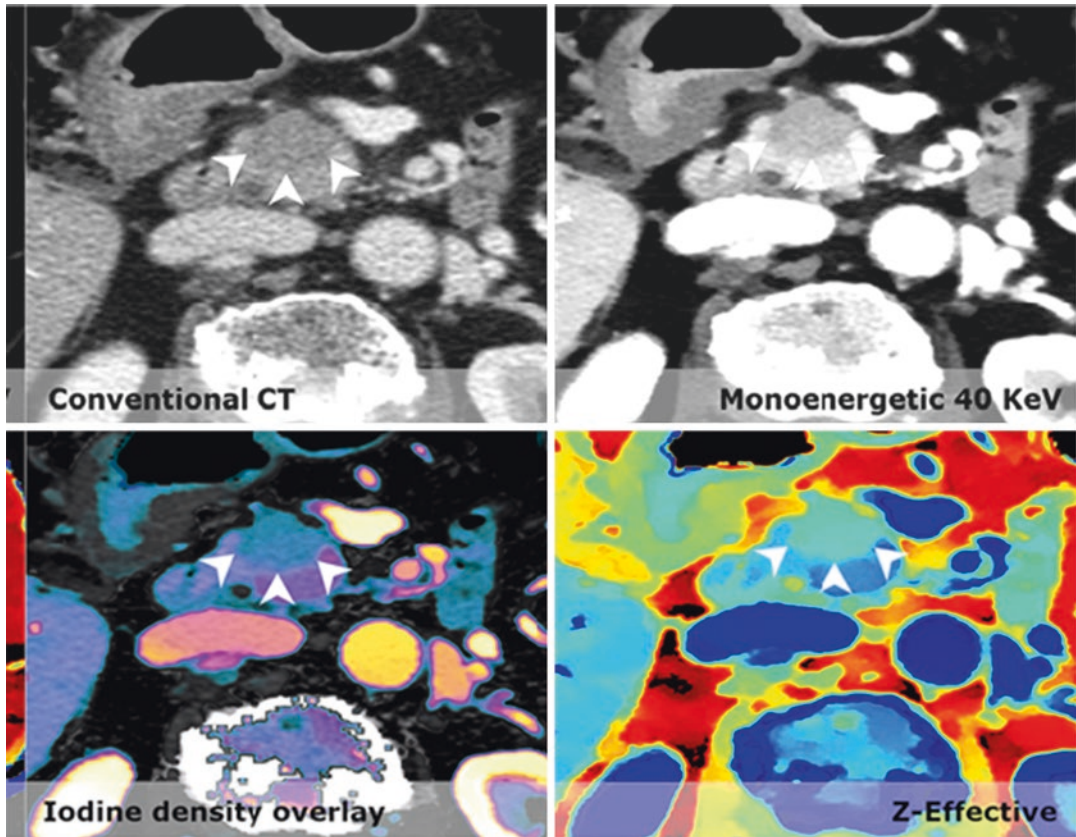


**Fig. 7** Patient with a slight increase in volume in the head of the pancreas and stranding in the peripancreatic fat. In the pancreatic head, a slight hypodense lesion (arrowheads outline the lesion) is visible on the conventional image; however, it is easily missed. On iodine density as

well as mono 40 keV and Zeff images, the lesion stands out against the normal pancreatic parenchyma and the lesion was correctly diagnosed as a pancreatic adenocarcinoma (Brun Andersen et al. 2020)

### 3.7 Iodine Removed [HU]

An image type in which all the voxels which are classified as not including iodine above a certain threshold are displayed as black voxels. All other voxels remain identical to MonoE 70 keV.

### 3.8 Uric Acid and Uric Acid Removed Pair [HU]

In these two spectral results, the classification is done between uric acid and calcium voxels and the two results are complementary with each other.

#### 3.8.1 Uric Acid [HU]

In the uric acid result, all the voxels which are classified as including uric acid remain identical to MonoE 70 keV. All other voxels classified as not including uric acid are displayed as black voxels.

#### 3.8.2 Uric Acid Removed [HU]

In the uric acid removed result, all the voxels which are classified as not including uric acid remain identical to MonoE 70 keV. All other voxels classified as including uric acid are displayed as black voxels.

The uric acid and uric acid removed image pair are intended for uric acid and calcium classifica-

tion and therefore have a potential use in gout disease diagnosis and stone characterization.

In gout disease, the attenuation of low-atomic-weight monosodium urate (MSU) crystals differs from that of high-atomic-weight calcium such as calcium pyrophosphate dihydrate (CPPD) crystals, that exist in pseudogout and can have a clinical presentation like that of gout.

Uric acid-calcium pairs are also useful in characterizing urinary calculus composition as demonstrated by Rajiah et al. (2017b).

The last two spectral results that are described below, Z effective and electron density can be used for material characterization.

### 3.9 Z Effective

This is an image in which the voxel values represent the effective atomic number of the displayed tissue. While the atomic number is characteristic of an element, the effective atomic number is characteristic of materials consisting of more than one element such as water, soft tissue, and bone.

A Z effective calculation is based on the ratio of attenuations at two different energies and is therefore independent of the material density. The expected Zeff values for known different tissues from the literature were calculated and a conversion curve between the monoEs ratio and the calculated Z effective was created.

The Z effective images can be displayed in color or gray scales. The dynamic range is set to be between 5 and 30, where water is 7.4 and air is set to be zero. Non-enhanced soft tissues have Z effective value of approximately seven. Fatty tissues have lower Z effective than water, while bone and contrast-enhanced tissues have higher values compared with water Z effective. Metal implants have a high Z effective possibly higher than 30.

In a phantom study (Hua et al. 2018), different tissues with different Z effective values from approximately 6 (adipose tissue) to about 13 (cortical bone) were scanned in different configura-

tions. It was found that the accuracy of the Z effective is on the order of  $\pm 2\%$  for both soft tissue and bone-equivalent materials, with somewhat larger percentage deviations for lung-mimicking materials. The accuracies were found to be similar in different scans and reconstruction parameters.

Z Effective images have the potential to differentiate tissues based on their atomic number values, for example, in stone characterization (Fulton et al. 2017). This is shown in Fig. 8 in a different study. In addition, it was shown that the use of contrast-enhanced spectral CT including Z effective images increases the confidence of the radiologists in correctly characterizing various lesions and minimizes the need for supplementary examinations (Brun Andersen et al. 2020). See Fig. 8.

The benefit of the dual-layer spectral CT was recently demonstrated in the emergency department (Demirler Simsir et al. 2020). It was shown that by using iodine density and Zeff maps, the detection of subtle filling defects and demonstration of the presence or lack of lung perfusion deficits in pulmonary embolism is better. This is shown in Fig. 9.

### 3.10 Electron Density [%EDW]

This is a spectral result that displays the electron density of each voxel relative to the electron density of water ( $3.34 \times 10^{29}$  electrons  $\times$  m<sup>-3</sup>) in units of percent where the expected value for water in these units is 100 [%EDW].

The electron density (ED) estimation is based on a linear combination of the photo-electric effect and Compton scattering where the Compton scattering component dominates. The two parameters of the linear combination coefficients were determined by finding the best fit to the expected electron densities of known literature tissues. The normalization was chosen so that the relative ED of water is 100.

For several decades, in order to calculate the radiation dose distribution, HU were converted to

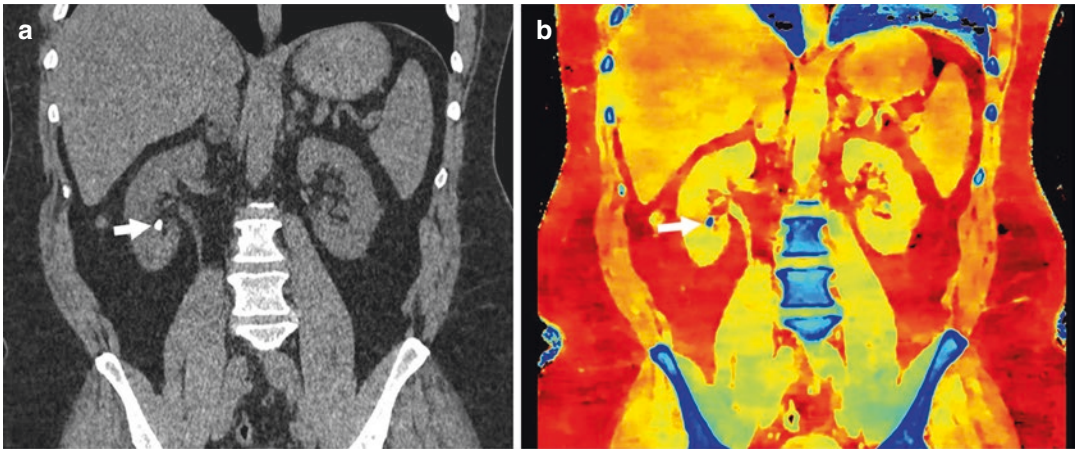


**Fig. 8** Urinary calculus composition. (a) Coronal 120-kVp routine diagnostic image in a patient with acute abdominal pain shows a 7-mm calculus in the inferior pole of the right kidney (arrow). (b) Effective atomic

number-based reconstruction at the same level shows that the calculus has high atomic number (arrow) consistent with a calcium calculus (Rassouli et al. 2017)

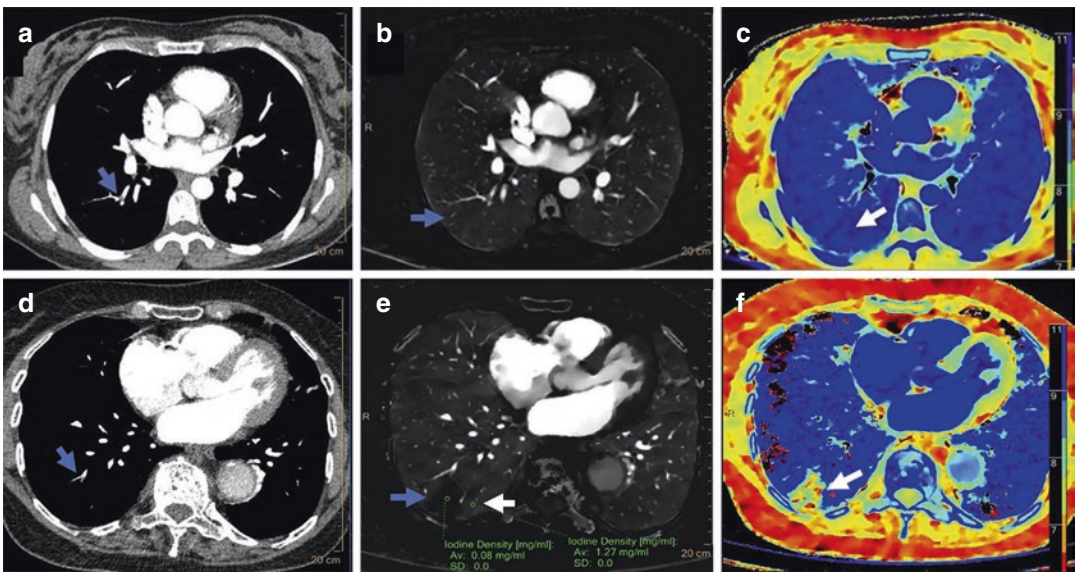


**Fig. 9** A 36-year-old woman presented with right-sided acute chest pain (upper row). (a) On conventional CT, a small filling defect was present in right lower lobe sub-segmental pulmonary artery (arrow). (b) Iodine density and (c) Zeff maps showed no perfusion deficit distal to the filling defect (arrows). A 90-year-old woman presented with dyspnea, right-sided chest pain (lower row), (d) Conventional CT, small filling defect was present in right lower lobe sub-segmental pulmonary artery (arrow). (e)

Iodine density map demonstrated a wedge-shaped area of decreased perfusion (iodine density; 0.08 mg/ml; blue arrow) compared to the adjacent lung parenchyma (iodine density; 1.27 mg/ml; white arrow) indicating a sub-segmental pulmonary embolism with perfusion deficit. (f) The Zeff map demonstrated the wedge-shaped area with decreased perfusion color-coded in light blue, yellow, and red (arrow) (Demirler Simsir et al. 2020)

the electron or physical density via a calibration curve, in the case of photon therapy or to the proton stopping power, in the case of proton therapy.

Dual-layer CT allows a direct calculation of the electron density on a pixel-by-pixel basis. This approach can potentially enhance the workflow of radiation therapy planning by eliminating the need for a calibration curve mapping for photon therapy and improve the range accuracy for proton therapy.

The accuracy of the electron density was assessed recently in phantoms studies (Hua et al. 2018; Rassouli et al. 2017). Hua et al. concluded that the electron density accuracy is of the order of  $\pm 1\%$  for both soft tissue and bone-equivalent materials and did not appear to be sensitive to different scans and reconstruction parameters. Ohira et al. (2019) found that percentage error of the electron density for each reference material varied from  $-2.0\%$  to  $1.2\%$  and therefore the use of dual-layer spectral CT can enhance radiotherapy treatment planning. In another study, it was demonstrated that in homogeneous and heterogeneous phantoms, the use of electron density and Z effective can improve the accuracy of the stopping power ratio (SPR) predictions for particle therapy resulting in remaining discrepancies in the order of  $1\%$ . This can minimize the beam range uncertainty and allow for reduced safety margins in the patient (Faller et al. 2020).

Recently, it was demonstrated on few case reports that ED imaging improves GGO visualization compared with conventional CT. It was suggested that ED imaging may improve the detection of early-stage COVID-19, a stage for which conventional CT has shown limited sensitivity for detection (Daoud et al. 2020).

### Compliance with Ethical Standards

**Disclosure of Interests** All authors are Philips employees.

**Ethical Approval** This article does not contain any studies with human participants performed by any of the authors.

**Ethical Approval** This article does not contain any studies with animals performed by any of the authors.

## References

- Abdullayev N et al (2019) Improvements of diagnostic accuracy and visualization of vertebral metastasis using multi-level virtual non-calcium reconstructions from dual-layer spectral detector computed tomography. *Eur Radiol* 29(11):5941–5949
- Altman A, Shapiro O, Levene S, et al. (2006) Double decker detector for spectral CT. US States Patent US 7,968,853
- Altman A, Goshen L, Shechter G, Brown K, Yagil Y, Katchalski T, Carmi R, Proksa R, Thran A, Brendel B, Daerr H, Romman Z (2015) From a dual-energy spectral detector to photon-counting, and the benefit of multi energy-bins detectors. CERN SpecsXray Workshop April 2015
- Alvarez RE (2011) Estimator for photon counting energy selective x-ray imaging with multi-bin pulse height analysis. *Med Phys* 38(5):2324–2334
- Alvarez RE, Macovski A (1976) Energy-selective reconstruction in X-ray computerized tomography. *Phys Med Biol* 21(5):733–744
- Ananthakrishnan L et al (2017) Spectral detector CT-derived virtual noncontrast images: comparison of attenuation values with unenhanced CT. *Abdom Radiol* 42(3):702–709
- Borggreffe J et al (2019) Accuracy of iodine density thresholds for the separation of vertebral bone metastases from healthy-appearing trabecular bone in spectral detector computed tomography. *Eur Radiol* 29(6):3253–3261
- Brooks RA, Di Chiro G (1978) Split detector computed tomography: a preliminary report. *Radiology* 126(1):255–257
- Brun Andersen M et al (2020) Impact of spectral body imaging in patients suspected for occult cancer: a prospective study of 503 patients. *Eur Radiol* 30(10):5539–5550
- Carmi R, Naveh G, Altman A (2005) Material separation with dual-layer CT. Presented at the IEEE-MIC Conference. Puerto Rico: Wyndham El Conquistador; 23–29 Oct 2005. First, and original presentation of the 2D scatter-plot based dual-energy material decomposition method in image plane. See also US PATENT: US7,778,380 B2, 2010, by the same authors
- Daoud B et al (2020) Could spectral CT have a potential benefit in coronavirus disease (COVID-19)? *Am J Roentgenol* 216(2):349–354
- Demirler S, Sinsir B, Danse E, Coche E (2020) Benefit of dual-layer spectral CT in emergency imaging of different organ systems. *Clin Radiol*
- Ehn S et al (2017) Assessment of quantification accuracy and image quality of a full-body dual-layer spectral CT system. *J Appl Clin Med Phys* 19(1):204–217
- Faller FK et al (2020) Pre-clinical evaluation of dual-layer spectral computed tomography-based stopping power prediction for particle therapy planning at the Heidelberg Ion Beam Therapy Center. *Phys Med Biol* 65(9):095007

- Fulton N et al (2017) Abdominal applications of a novel detector-based spectral CT. *Curr Probl Diagn Radiol* 47(2):110–118
- Große Hokamp N et al (2017a) Reduction of artifacts caused by orthopedic hardware in the spine in spectral detector CT examinations using virtual monoenergetic image reconstructions and metal-artifact-reduction algorithms. *Skeletal Radiol* 47(2):195–201
- Große Hokamp N et al (2017b) Assessment of arterially hyper-enhancing liver lesions using virtual monoenergetic images from spectral detector CT: phantom and patient experience. *Abdom Radiol* 43(8):2066–2074
- Große Hokamp N et al (2018) Artifact reduction from dental implants using virtual monoenergetic reconstructions from novel spectral detector CT. *Eur J Radiol* 104:136–142
- Große Hokamp N et al (2019) Stratification of pulmonary nodules using quantitative iodine maps from dual-energy computed tomography. *Am J Respir Crit Care Med* 199(2):e3–e4
- Hickethier T et al (2017) Fourth update on CT angiography of coronary stents: in vitro evaluation of 24 novel stent types. *Acta Radiol* 59(9):1060–1065
- Hickethier T et al (2020) Venous-phase chest CT with reduced contrast medium dose: Utilization of spectral low keV monoenergetic images improves image quality. *Eur J Radiol* 122:108756
- Hojjati M et al (2017) Quality of routine diagnostic abdominal images generated from a novel detector-based spectral CT scanner: a technical report on a phantom and clinical study. *Abdom Radiol* 42(11):2752–2759
- Hua C-H et al (2018) Accuracy of electron density, effective atomic number, and iodine concentration determination with a dual-layer dual-energy computed tomography system. *Med Phys* 45(6):2486–2497
- Jamali S et al (2019) Virtual unenhanced phase with spectral dual-energy CT: is it an alternative to conventional true unenhanced phase for abdominal tissues? *Diagn Interv Imaging* 100(9):503–511
- Kaltsz K et al (2017) Noise characteristics of virtual monoenergetic images from a novel detector based spectral CT scanner. *Eur J Radiol* 98:118–125
- Kikano EG et al (2020) Utility of iodine density perfusion maps from dual-energy spectral detector CT in evaluating cardiothoracic conditions: a primer for the radiologist. *Am J Roentgenol* 214(4):775–785
- Lennartz S et al (2018) Dual-layer detector CT of the head: initial experience in visualization of intracranial hemorrhage and hypodense brain lesions using virtual monoenergetic images. *Eur J Radiol* 108:177–183
- Lennartz S et al (2019) Diagnostic value of spectral reconstructions in detecting incidental skeletal muscle metastases in CT staging examinations. *Cancer Imaging* 19(1):50
- Liu J-J et al (2019) Improved visualization of gastric cancer and increased diagnostic performance in lesion depiction and depth identification using monoenergetic reconstructions from a novel dual-layer spectral detector CT. *Acad Radiol* 27(6):e140–e147
- Nadjiri J et al (2018) Accuracy of calcium scoring calculated from contrast-enhanced coronary computed tomography angiography using a dual-layer spectral CT: a comparison of calcium scoring from real and virtual non-contrast data. *PLoS One* 13(12):e0208588
- Nagayama Y et al (2017) Dual-layer DECT for multiphase hepatic CT with 50 percent iodine load: a matched-pair comparison with a 120 kVp protocol. *Eur Radiol* 28(4):1719–1730
- Neuhaus V et al (2017a) Improvement of image quality in unenhanced dual-layer CT of the head using virtual monoenergetic images compared with polyenergetic single-energy CT. *Invest Radiol* 52(8):470–476
- Neuhaus V et al (2017b) Metal artifact reduction by dual-layer computed tomography using virtual monoenergetic images. *Eur J Radiol* 93:143–148
- Neuhaus V et al (2017c) Improvement of image quality in unenhanced dual-layer CT of the head using virtual monoenergetic images compared with polyenergetic single-energy CT. *Invest Radiol* 52(8):470–476
- Neuhaus V et al (2018) Bone marrow edema in traumatic vertebral compression fractures: Diagnostic accuracy of dual-layer detector CT using calcium suppressed images. *Eur J Radiol* 105:216–220
- Oda S et al (2018) Low contrast material dose coronary computed tomographic angiography using a dual-layer spectral detector system in patients at risk for contrast induced nephropathy. *Br J Radiol* 92(1094):20180215
- Ohira S et al (2019) Estimation of electron density, effective atomic number and stopping power ratio using dual-layer computed tomography for radiotherapy treatment planning. *Phys Med* 56:34–40
- Rajiah P et al (2017a) Spectral detector CT for cardiovascular applications. *Diagn Interv Radiol* 23(3):187–193
- Rajiah P et al (2017b) Benefit and clinical significance of retrospectively obtained spectral data with a novel detector-based spectral computed tomography – initial experiences and results. *Clin Imaging* 49:65–72
- Rassouli N et al (2017) Detector-based spectral CT with a novel dual-layer technology: principles and applications. *Insights Imaging* 8(6):589–598
- Reimer RP et al (2019) Virtual monoenergetic images from spectral detector CT enable radiation dose reduction in unenhanced cranial CT. *AJNR Am J Neuroradiol* 40(10):1617–1623
- Sauter AP et al (2018) Dual-layer spectral computed tomography: virtual non-contrast in comparison to true non-contrast images. *Eur J Radiol* 104:108–114
- Sellerer T et al (2018) Dual-energy CT: a phantom comparison of different platforms for abdominal imaging. *Euro Radiology* 28(7):2745–2755. <https://doi.org/10.1007/s00330-017-5238-5>
- Tsang DS et al (2017) Quantifying potential reduction in contrast dose with monoenergetic images synthesized from dual-layer detector spectral CT. *Br J Radiol* 90(1078):20170290

- Van Hedent S et al (2018) Effect of virtual monoenergetic images from spectral detector computed tomography on coronary calcium blooming. *J Comput Assist Tomogr* 42(6):912–918
- Van Ommen F et al (2018) Image quality of conventional images of dual-layer SPECTRAL CT: a phantom study. *Med Phys* 45(7):3031–3042
- Wellenberg RHH et al (2017) Quantifying metal artefact reduction using virtual monochromatic dual-layer detector spectral CT imaging in unilateral and bilateral total hip prostheses. *Eur J Radiol* 88:61–70
- Yoon JH et al (2020) Double low-dose dual-energy liver CT in patients at high-risk of HCC. *Invest Radiol* 55(6):340–348
- Zhang X et al (2020) Evaluating the temporomandibular joint disc using calcium-suppressed technique in dual-layer detector computed tomography. *J Int Med Res* 48(3):300060519891332